

# Synthesis of interconnected graphene framework with two-dimensional protective layers for stable lithium metal anodes

Xiao Nie<sup>a,1</sup>, Anyi Zhang<sup>a,1</sup>, Yihang Liu<sup>b</sup>, Chenfei Shen<sup>a</sup>, Mingrui Chen<sup>a</sup>, Chi Xu<sup>c</sup>, Qingzhou Liu<sup>a</sup>, Jiansong Cai<sup>a</sup>, Abdulrahman Alfaraidi<sup>a</sup>, Chongwu Zhou<sup>b,\*</sup>

<sup>a</sup> Mork Family Department of Chemical Engineering and Materials Science, University of Southern California, Los Angeles, CA 90089, United States

<sup>b</sup> Ming Hsieh Department of Electrical Engineering, University of Southern California, Los Angeles, CA 90089, United States

<sup>c</sup> Department of Physics and Astronomy, University of Southern California, Los Angeles, CA 90089, United States

## ARTICLE INFO

### Keywords:

Lithium metal anodes

Graphene framework

Three-dimensional current collector

## ABSTRACT

Severe lithium (Li) dendrite growth during the plating/stripping process, which results in low Coulombic efficiency and safety issues, strongly hinders the practical applications of Li metal anodes. Herein, we propose a novel design of three-dimensional (3D) interconnected graphene (IG) framework synthesized with the help of nickel (Ni) microspheres for stable Li metal anodes. The as-prepared IG framework consists of multiple stacks of two-dimensional (2D) graphene layers and plenty of hollow graphene microspheres in between, and thus provides protective layers on the top to suppress lithium dendrites, sufficient surface area to reduce the effective current density, as well as ion channels for fast Li transport, which is confirmed by post-cycle morphology characterization. When Li foil was used as the counter electrode for Li deposition, the assembled coin cell maintained an average Coulombic efficiency of more than 97.5% for 100 cycles at current density of 1 mA cm<sup>-2</sup> with a Li loading of 1 mAh cm<sup>-2</sup>. Furthermore, we achieved stable cycling for more than 300 h at a current density of 1 mA cm<sup>-2</sup> with a Li loading of 2 mAh cm<sup>-2</sup> when assembled as symmetric cells. This strategy of vertically stacking 2D materials provides a novel approach towards dendrite-free Li metal anodes for the next-generation energy storage systems.

## 1. Introduction

Lithium ion batteries (LIBs) have been successfully used in portable electronics and electric vehicles for many years [1–3]. Although the demand for high-energy-density keeps increasing, the existing commercial LIB systems are getting close to their theoretical capacity limits. In order to push the energy density to an even higher level, Li metal anodes, which can be paired up with sulfur [4–7], air [8–10] and transition metal oxide cathodes [1,2,11,12], have been intensively studied recently. Compared with graphite and silicon anodes [13,14], lithium metal anodes show a number of advantages: [15,16] (1) the highest theoretical capacity (3860 mAh g<sup>-1</sup> or 2061 mAh cm<sup>-3</sup>); (2) the most negative electrochemical potential (-3.04 V vs. the standard hydrogen electrode); (3) containing lithium, which means that no pre-lithiation process is needed when paired up with lithium-free cathodes like sulfur and air. However, the use of Li metal anodes is hindered by several obstacles. Generally speaking, the formation of Li dendrites during cycling, which leads to capacity fading and severe

safety issues, is considered as the primary challenge to overcome [17–19]. Although there is still no agreement about the Li dendrite growth mechanism, one popular theory suggests that the dendritic growth is mainly caused by non-uniform local ion concentration [18,20]. When Li metal reacts with organic solvents and Li salts in the electrolyte, an electrically insulating but ionic conductive layer will be formed, which is called solid-electrolyte interface (SEI) [21,22]. Due to the localized ion concentration gradient, the thickness of the SEI layer is very uneven throughout the surface. Considering the large volume expansion of Li during the plating process, locations with a thinner SEI layer will first fracture and the fresh Li metal will be exposed to the electrolyte. The exposed parts will grow faster than others, resulting in ramified morphology. When the Li dendrites are long enough, they can easily puncture the separator, resulting in short circuit or even an explosion. What's worse is that the volume contraction of Li during stripping processes will further crack the SEI around Li dendrites. In this way, a lot of Li dendrites will become electrically isolated from the substrate, which is so-called 'dead' Li. The dead Li

\* Corresponding author.

E-mail address: [chongwuz@usc.edu](mailto:chongwuz@usc.edu) (C. Zhou).

<sup>1</sup> Contribute equally in this work.

<https://doi.org/10.1016/j.ensm.2018.09.028>

Received 18 June 2018; Received in revised form 14 September 2018; Accepted 29 September 2018

2405-8297/ © 2018 Elsevier B.V. All rights reserved.

can no longer be utilized, leading to low Coulombic efficiency.

The current collector is regarded as a key component in Li metal anodes, and can make significant impact on the deposited Li metal morphology as well as the electrochemical performance. Therefore, a lot of effort has been made to modify current collectors for stable Li metal deposition. Because one main factor that leads to Li dendrite formation is inhomogeneous Li-ion flux distribution, it is straightforward to design a three-dimensional (3D) current collector that can increase the surface area and reduce the effective current density on the electrode. Following this strategy, 3D porous metal foil [23–26], porous graphene framework [27–29] and carbon nanofiber/nanotube network [30–36] are demonstrated to suppress dendrite growth and improve Coulombic efficiency effectively. However, this strategy can only reduce the growth rate of Li dendrites to some extent. After long cycles, mossy surface morphology can still be formed. In addition, another approach is to use a chemically stable and mechanically strong thin layer, such as interconnected hollow carbon nanospheres [37] and two-dimensional (2D) materials (including grapheme [38], hexagonal boron nitride [38] and molybdenum disulfide [39]), as interfacial layer. During cycling, the interfacial layer can constrain Li deposition underneath it, leading to flat surface morphology. Nevertheless, one single thin protection layer may not be sufficient when the Li metal loading is high. Additionally, if the ion conductivity of the protection layer is low, it's hard to achieve good cycling performance at high current densities.

Inspired by the previous reports, we rationally designed an interconnected graphene (IG) framework consisting of both 3D graphene hollow spheres and 2D graphene flakes. The 3D graphene hollow spheres were used to increase the surface area and provide enough ion-transport channels. The 2D graphene flakes worked as interfacial layers to flatten the surface morphology and suppress dendrite growth. Using the IG current collector, we demonstrated highly reversible Li plating/stripping with an average Coulombic efficiency of 97.5% over 100 cycles at a current density of  $1 \text{ mA cm}^{-2}$  for a total of  $1 \text{ mAh cm}^{-2}$  of Li. In addition, the symmetric cell presented stable voltage profiles with small hysteresis up to 300 h, indicating the formation of stable SEI. Based on detailed characterizations, we believe that the innovative structure of the IG current collector plays an important role in the improvement of the performance, which brings about a promising route to tackle the intrinsic issues of Li metal anodes.

## 2. Results and discussion

We used a rather scalable method to prepare the 3D IG framework. Fig. 1 illustrates the schematic of the preparation process and corresponding SEM images after each step during the synthesis. Fig. 1a shows the general preparation process. The vacuum filtration was utilized to get the composite film consisting of multiple layers of graphene oxide (GO) and abundant nickel (Ni) microspheres, whose diameter is in the range of  $0.5\text{--}1 \mu\text{m}$ . The surface of the film was covered by large GO flakes (as shown in Fig. S1a) and the Ni spheres were dispersed between two GO layers (as shown in Fig. 1b). The thickness of the composite film is about  $25 \mu\text{m}$  according to the side-view SEM images (Fig. S2a). After vacuum filtration, the composite film was punched to small circular disks with an area of  $1.5 \text{ cm}^2$ . Then, the small circular disks were loaded into a furnace for graphene chemical vapor deposition (CVD) [40–43], using methane ( $\text{CH}_4$ ) as carbon source and argon (Ar) as carrier gas, and graphene was grown on the surface of Ni microspheres (Fig. 1c and Fig. S1b). The thickness of the film increased to about  $30 \mu\text{m}$  according to the side-view SEM image shown in Fig. S2b. Afterwards, the obtained samples were immersed in Ni etchants to etch the Ni microspheres away. As a result, massive hollow graphene spheres were distributed in between each two graphene layers. From the side-view SEM image in Fig. 1d, the edges of the 2D graphene flakes can be clearly observed; however, we can only see the top surface of the 2D graphene flakes in the top-view SEM image in Fig. S1c. In this way, a freestanding and binder-free IG

framework was produced, consisting of vertically stacked 2D graphene flakes together with sufficient void space. From the side view we can see that the thickness of the as-prepared sample is still about  $30 \mu\text{m}$  (Fig. S2c), and most of the graphene hollow spheres are porous, which is good for Li ion transport during cycling.

The Raman data in Fig. 2a exhibits more information about samples after vacuum filtration, graphene CVD, and Ni etching. In the spectrum of the sample after vacuum filtration, the D-band (at about  $1300 \text{ cm}^{-1}$ ) and G-band (at about  $1600 \text{ cm}^{-1}$ ) were broad, and the 2D band (at  $2700 \text{ cm}^{-1}$ ) did not exist, which is typical for Raman spectra of GO [44]. After CVD, the D-band and G-band became narrower, and the 2D-band appeared, indicating the successful synthesis of a graphene framework after the CVD process [45]. Also, the ratio of intensity of the G-band and 2D-band suggests the existence of few-layer graphene. During the CVD process, few-layer graphene was grown on Ni spheres and the 2D GO flakes were reduced to 2D graphene flakes at the same time, which is consistent with the Raman spectrum. The presence of D-band indicates that the GO flakes were not completely reduced and there were still some oxygen containing functional groups left. After Ni was etched away, the overall Raman spectrum almost did not change, but the D-band intensity increased a little bit, probably due to some defects created during the etching process. The X-ray photoelectron spectroscopy (XPS) measurement was also performed to study the change of the surface chemistry after each step during the preparation process. The XPS spectrum of the sample after vacuum filtration, which is depicted in Fig. S3a, can be separated into three peaks ( $284.8 \text{ eV}$ ,  $286.8 \text{ eV}$  and  $288.0 \text{ eV}$ ). These three peaks can be assigned to C-C, C-O and O-C=O, respectively [46]. Samples after CVD (Fig. S3b) and after etching (Fig. S3c) have similar XPS spectra and they can be divided into two peaks ( $284.8 \text{ eV}$  and  $285.1 \text{ eV}$ ), representing the bonding of C-C and C-O, respectively. It also confirms the conclusion from the Raman spectroscopy.

In order to gain further insight into the morphology of graphene hollow spheres grown on Ni, we used transmission electron microscope (TEM) to characterize samples after CVD and after etching (shown in Fig. 2 and Fig. S4). Fig. S4a shows the low-magnification TEM image of the sample after CVD. One can clearly see that the structure of “graphene oxide layer-Ni spheres-graphene oxide layer” is still maintained after graphene CVD. While in high magnification, the graphene layer whose thickness is  $\sim 10 \text{ nm}$  can be observed on the surface of the Ni spheres (Fig. S4b and Fig. 2b). After Ni etching, graphene hollow spheres can be clearly observed and the thickness of the graphene shell kept similar to the thickness of samples before etching (shown in Figs. S4c and 2c). Fig. 2d to Fig. 2f present the scanning transmission electron microscopy (STEM) images and corresponding energy-dispersive X-ray spectroscopy (EDX) mapping data of the samples after Ni etching, which gives us information about element distribution. It is clear that the major element of the sphere is C, and Ni is only in a very small amount, which is consistent with the data shown in Fig. S5 given by SEM EDX measurement. The atomic ratio of Ni was 35.2% before etching and it decreased to less than 1% after the sample was immersed in Ni etchant for 40 min. The remaining trace amount of Ni may serve as Li nucleation seeds for stable Li deposition [47,48].

The unique structure of our 3D IG shows potential to be utilized for stable Li metal anodes. Fig. 3a and b illustrate our hypothesis of Li metal deposition behavior on planar Cu foils and IG. When Li metal is deposited onto Cu foils directly, Li dendrites will be formed. As the Li dendrites grow longer and longer after several cycles, some of them will lose electrical conduction and become dead Li. The dead Li cannot be stripped any longer, resulting in reduced Coulombic efficiencies. Furthermore, the Li dendrite can also puncture the separators, leading to short circuit and severe safety problems. On the other hand, when Li metal is deposited onto a 3D IG current collector, the effective current density would decrease due to the increased effective surface area, reducing the probability of Li dendrite formation. Even though some dendrites may still be formed occasionally, they would be suppressed

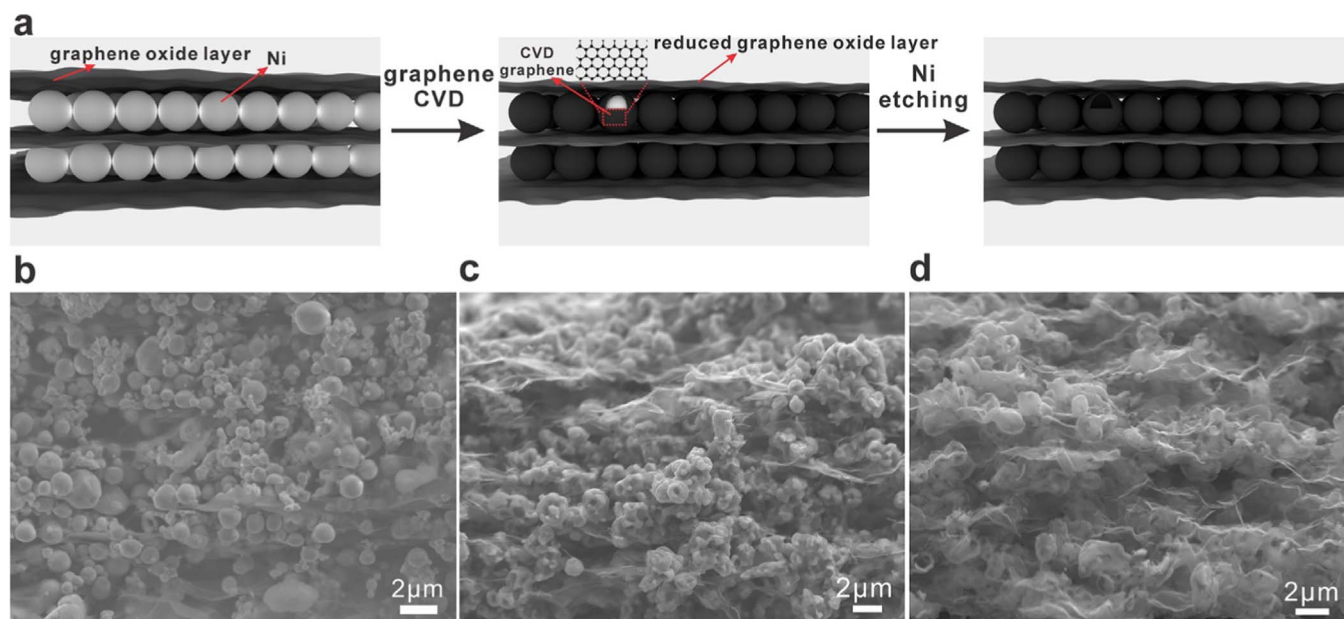


**Fig. 1.** Schematic of the preparation process of the 3D IG framework and the corresponding side-view SEM images after each step. (a) the schematic of preparation of the 3D IG framework; Side-view SEM images of the sample (b) after vacuum filtration, (c) after graphene CVD, and (d) after Ni etching.

by the planar 2D graphene layers at the early stage. Therefore, we are able to achieve more stable Li deposition with high Coulombic efficiencies and flat surface morphology. The electrochemical behavior of Li plating/stripping on 3D IG was examined in coin cells and the pristine Cu foil was tested as a control sample. Li foils were used as the counter electrodes, and 1 M lithium bis(trifluoromethanesulfonyl) imide (LiTFSI) in 1,2-dimethoxyethane (DME) and 1,3-dioxolane (DOL) (volume ratio 1:1) with 0.2 M lithium nitrate ( $\text{LiNO}_3$ ) as additive was used as the electrolyte. In each cycle, the batteries were first discharged for 1 h and then charged to 1 V at a constant current density of  $1 \text{ mA/cm}^2$ . Fig. 3c shows the cycling performance of a planar Cu current collector and a 3D IG current collector. The Coulombic efficiency of 3D IG electrode kept increasing in the first 5 cycles, which can be attributed to the formation of solid electrolyte interface (SEI), and then maintained at a high level up to 100 cycles. The overall average Coulombic efficiency was 97.5% and the average Coulombic efficiency after 5 cycles was as high as 98.5%. In comparison, the Coulombic efficiency of bare Cu electrode maintained above 90% in the early stage, but degraded dramatically after 30 cycles. After 90 cycles, the Coulombic efficiency was as low as about 20%. Obviously, the 3D IG showed much better electrochemical performance of Li plating/stripping, which is consistent with our hypothesis. The discharge/charge curves of the IG electrode are shown in Fig. 3d. In the first 10 cycles, the formation of SEI consumed part of plated Li, leading to the relatively low Coulombic efficiency in the discharge/charge curve. Afterwards, the Coulombic efficiency was close to 100% from 20 cycles to 100 cycles, indicating that almost all the plated Li metal can be stripped reversely after the formation of stable SEI. Similar behaviors were observed when the current density was increased to  $2 \text{ mA cm}^{-2}$  (Fig. S6a), or when the Li loading was increased to  $2 \text{ mAh cm}^{-2}$  (Fig. S6b). At higher current density or higher Li loading, the 3D IG electrodes can still facilitate stable Li deposition in the first 100 cycles, and performed much better than the bare Cu electrode. The specific capacities are calculated to be  $2143 \text{ mAh g}^{-1}$  (with  $1 \text{ mAh cm}^{-2}$  Li loading) and  $4286 \text{ mAh g}^{-1}$  (with  $2 \text{ mAh cm}^{-2}$  Li loading) based on the total mass of IG current collector, which is much higher than the theoretical gravimetric capacity of graphite ( $372 \text{ mAh g}^{-1}$ ) [49]. In order to further investigate the cycling stability of Li metal anodes with different current collectors, we assembled symmetric cells using IG current collector with deposited Li as the working electrodes, and Li

foils as the counter electrodes. As control samples, we also assembled bare Cu current collectors with deposited Li as the working electrodes, and Li foils as the counter electrodes. The galvanostatic discharge/charge voltage profiles of symmetric cells with different current collectors are depicted in Fig. 3g and f. At  $1 \text{ mA cm}^{-2}$ , the Li metal anode with IG current collector exhibited excellent cycling stability with small overpotential and negligible voltage fluctuation up to 300 h, owing to the good electrode-electrolyte contact and uniform SEI layer. In contrast, the overpotential of the symmetric cell with a bare Cu current collector was much larger initially. After 75 h, the overpotential increased dramatically and the voltage profiles fluctuated a lot, which is related to non-uniform Li deposition and fractal dendrite formation [48]. Similar behaviors were observed when the current density was increased to  $2 \text{ mA cm}^{-2}$ . The Li metal anode with IG current collector showed stable voltage profiles up to 200 h; however, the overpotential of the Li metal anode with bare Cu current collector increased rapidly after 40 h, which is consistent with the symmetric cell tested at  $1 \text{ mA cm}^{-2}$ . In this way, we can confirm the advantageous electrochemical performance of Li metal anodes with IG current collector.

In order to study the post-cycle surface morphology of Li metal anodes, SEM was performed for both IG and bare Cu current collectors after 50 cycles. The top-view SEM images of deposited Li on IG at different magnifications are presented in Fig. 4a and b. After the 50th plating process, 2D graphene flakes and 3D graphene spheres can still be observed on the flat surface. Although a small amount of Li can still be deposited on the top of the 2D graphene flakes, it would not grow to long dendrites and its effect can be ignored. In the high-magnification image shown in Fig. 4b, we can even clearly observe some Li dendrites grown underneath the 2D graphene flakes. Those dendrites were constrained by the 2D graphene top layer and cannot grow longer, which resolved the dendrite formation problem in the early stage. In comparison, the top-view SEM image of IG after the 50th stripping process is shown in Fig. S7. The morphology is similar to the morphology after plating due to the presence of SEI, while we can still observe more void space in the image after stripping. We believe that the stable SEI layers formed during cycling play an important role in the improved cycling performance. In order to study the composition of the SEI layers, XPS was conducted for IG electrodes before cycling, after 5 cycles and after 50 cycles, as shown in Fig. S8. From the C 1s spectrum, the O-C=O peak increased a lot during cycling, suggesting that COOLi is the main functional group in



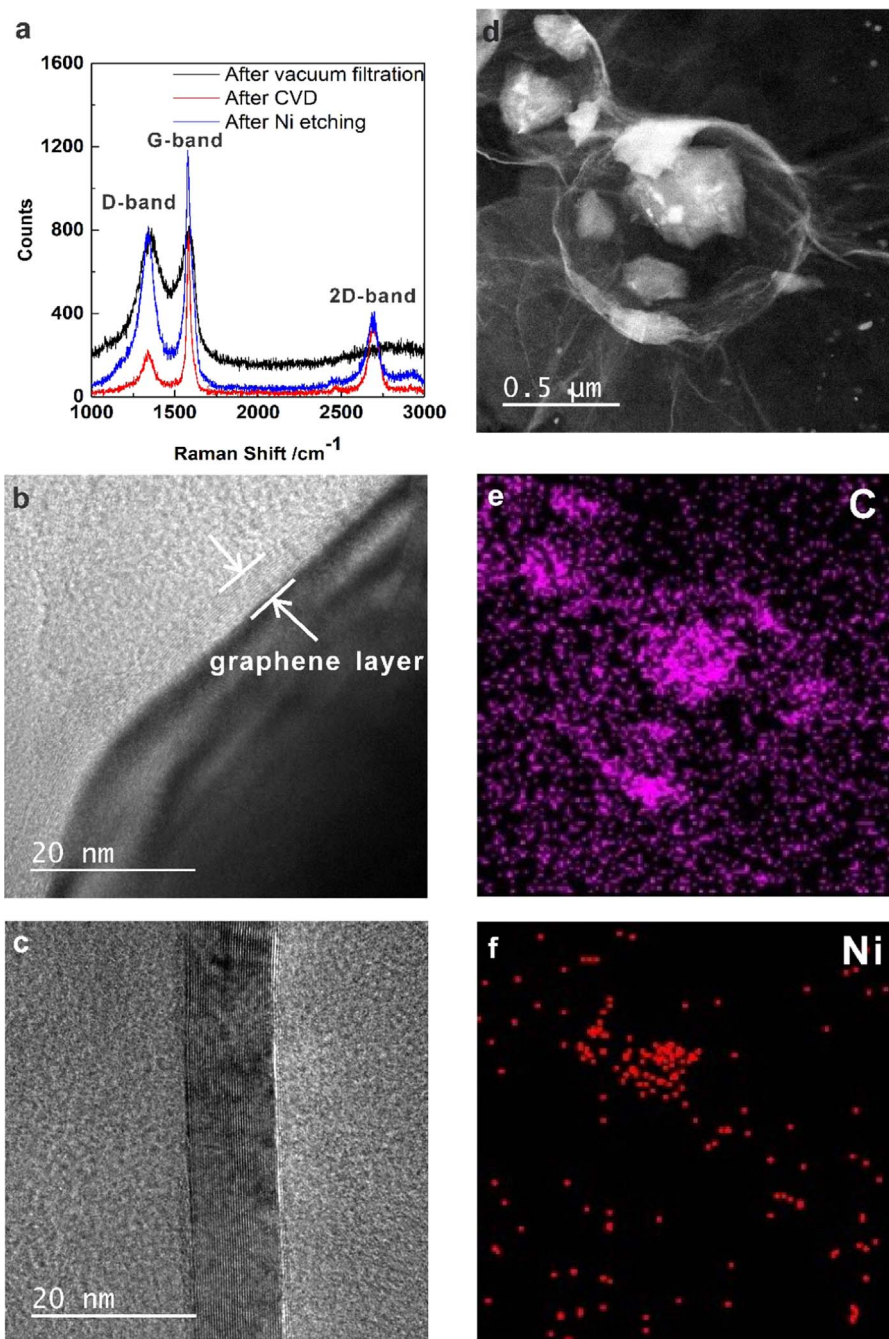


**Fig. 2.** Morphological study and characterization of 3D IG framework. (a) Raman spectra of samples after vacuum filtration, after graphene CVD and after Ni etching; High-resolution TEM images of the material (b) after graphene CVD and (c) after Ni etching; (d) the STEM image of the 3D IG framework and the corresponding EDX mapping of (e) C and (f) Ni.

the SEI [50,51]. From the F 1s spectrum, we can confirm the formation of LiF during cycling, which can work as a surface protection layer to suppress the Li dendrite growth [52,53]. Fig. 4c and d shows the post-cycle cross-section SEM images of a Li deposited IG current collector with different magnifications. After Li plating, the thickness of the IG increased to about 50  $\mu\text{m}$ , but the whole structure of the current collector can still be preserved thanks to the good flexibility of graphene. In the high-magnification image in Fig. 4d, the side edge of 2D graphene flakes can be clearly observed and deposited Li metal was sandwiched by two layers graphene. In addition, the deposited Li metal has particle-like morphology with a size of around 1  $\mu\text{m}$ , which is similar to the size of the hollow graphene spheres. This phenomenon suggests that in the early stage of deposition, Li ions nucleate inside or around the hollow graphene spheres, as well as on the 2D graphene flakes. As more Li

got deposited, the Li particles expanded and merged with each other. In this way, the presence of hollow graphene spheres can effectively increase the effective surface area. It is noticeable that the deposited Li metal is more likely to expand in the directions parallel to the 2D graphene flakes due to the physical confinement effect of the 2D flakes. In contrast, dendritic growth of Li is observed when Li metal was deposited onto a bare Cu current collector, as shown in Fig. 4e. The Li dendrites can be as long as several tens micrometers and their diameters are usually less than 5  $\mu\text{m}$ . These Li dendrites can either disconnect from the current collector and become dead Li, leading to reduced Coulombic efficiency, or easily puncture the separator, causing short circuit which may result in an explosion. In addition, the thickness of the deposited Li metal is as large as 120  $\mu\text{m}$ , which is more than two times of the deposited Li on IG. The increment

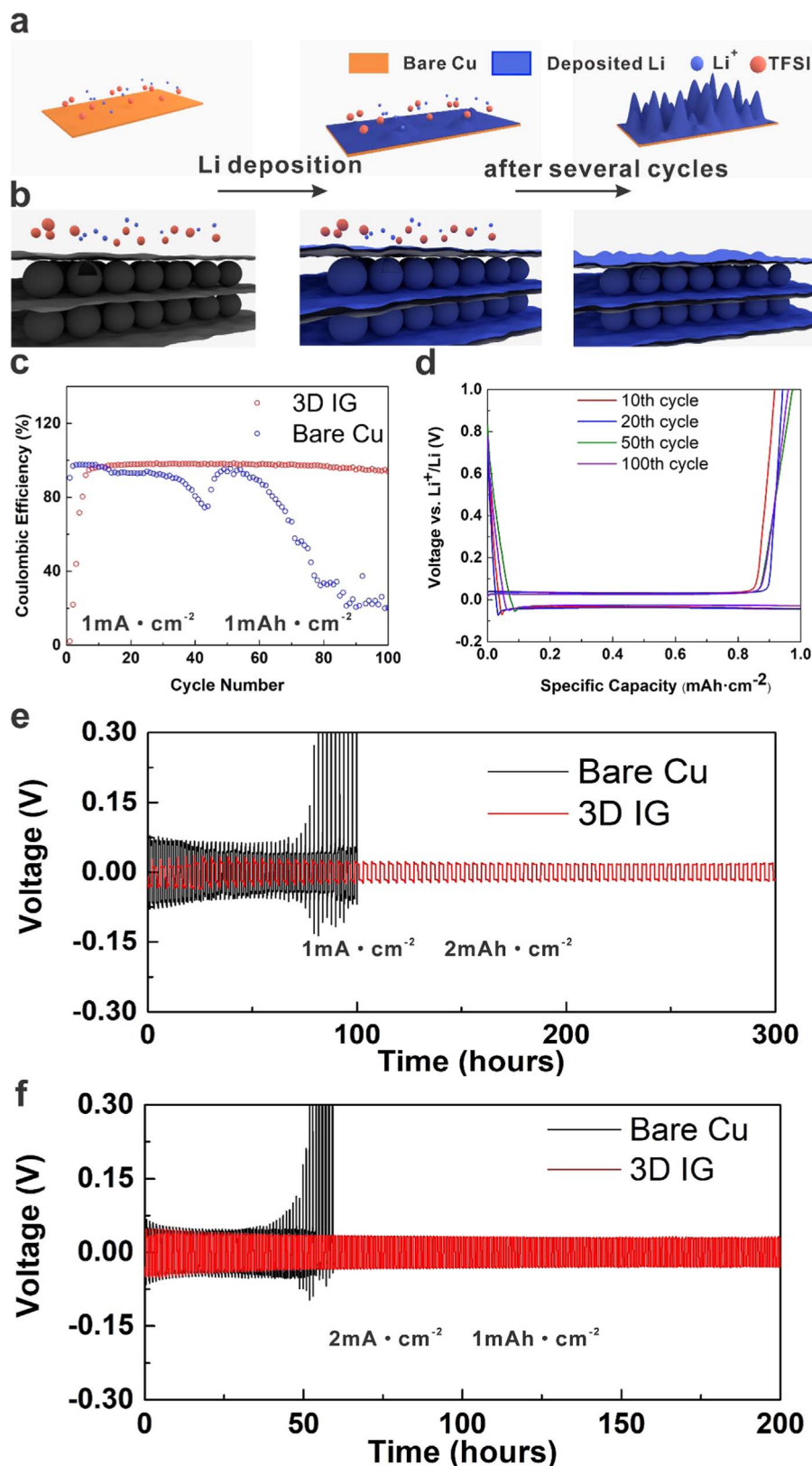


**Fig. 3.** Electrochemical performance of coin cells using bare Cu and as-prepared 3D IG as current collectors. Schematic of cycling using (a) bare Cu foil and (b) 3D IG as the current collector with Li metal foil as the counter electrode; (c) Cycling performance of 3D IG and bare Cu foil current collectors for 100 cycles at the current density of  $1 \text{ mA cm}^{-2}$  and a Li loading of  $1 \text{ mAh cm}^{-2}$ ; (d) Capacity-voltage profile of the battery shown in (c); Voltage profiles of symmetric cells using bare Cu and 3D IG as current collectors (e) at a current density of  $1 \text{ mA cm}^{-2}$  and Li loading of  $2 \text{ mAh cm}^{-2}$  and (f) at a current density of  $2 \text{ mA cm}^{-2}$  and Li loading of  $1 \text{ mAh cm}^{-2}$ .

in thickness further confirms that a large amount of dead Li lost connection with the current collector during cycling, leading to continuous volume expansion.

In order to gain insight into the growth of Li metal, electrochemical impedance spectroscopy (EIS) analysis of samples using different current collectors was performed (shown in Fig. 5). The semicircle at

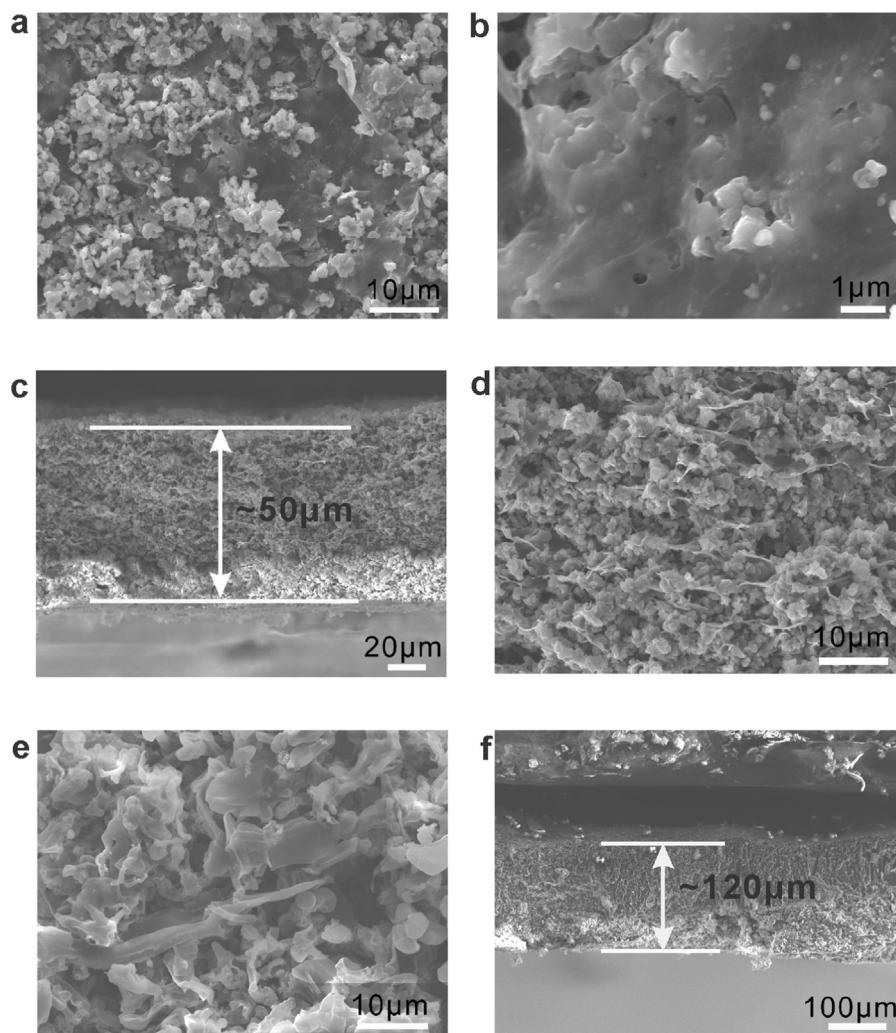


**Fig. 4.** Post-cycle morphology of 3D IG and bare Cu current collectors. (a), (b) Top-view SEM images of 3D IG electrode after the 50th plating process; (c), (d) Side-view SEM images of 3D IG electrode after the 50th plating process; (e) Top-view and (f) side-view SEM images of bare Cu foil after the 50th plating process.

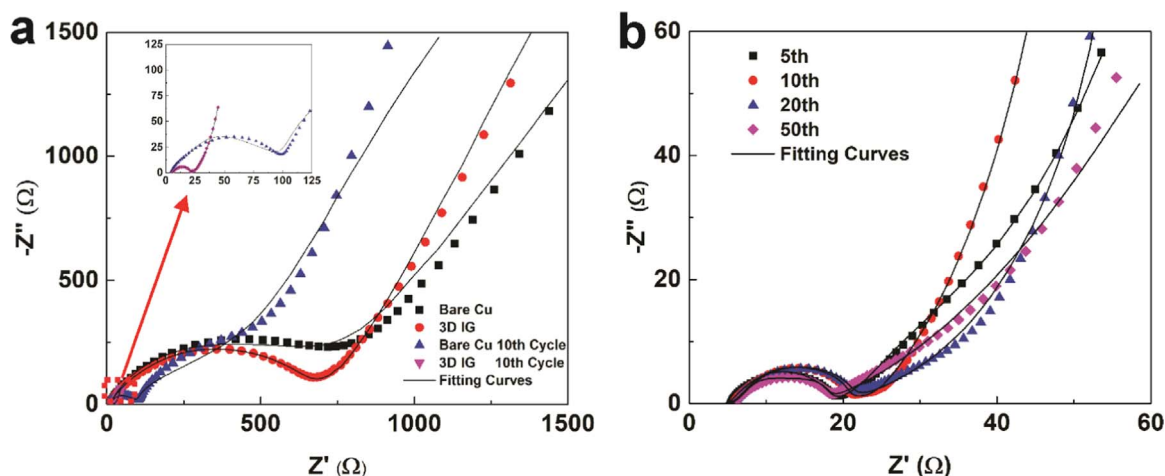


**Fig. 5.** Nyquist plots of impedance spectra of coin cells with fitting curves. (a) Impedance spectra and fitting curves of cells with 3D IG and bare Cu foil before cycling and after 10 cycles at a current density of  $1 \text{ mA cm}^{-2}$  and a Li loading of  $1 \text{ mAh cm}^{-2}$ . The inset is the magnified plots of the cells; (b) Impedance spectra and fitting curves of cells with 3D IG after the 5th, 10th, 20th and 50th cycles.

high and intermediate frequencies corresponds to the interfacial resistance of the electrode and electrolyte. Before cycling, the two kinds of current collectors exhibit similar spectra. However, the cell using a bare Cu current collector shows much large interfacial resistance than the cell using an IG current collector after 10 cycles,

indicating the formation of a thicker and non-uniform SEI. The impedance spectra evolution of the cell with an IG current collector is depicted in Fig. 5b. An equivalent circuit (Fig. S9a) was used to fit the measured data and the results of interfacial resistance are shown in Fig. S9b. It's worthy to note that there is almost no change in the



interfacial resistance (about 15  $\Omega$ ) from the 5th cycle to the 50th cycle, confirming that a stable SEI was formed during cycling. We believe that the 2D graphene flakes play a key role in the formation of a stable SEI, which is very important to improve the Coulombic efficiency and avoid short circuit.

### 3. Conclusion

In conclusion, we have demonstrated a novel design of 3D IG framework with vertically stacked 2D protective layers and its successful application for stable lithium metal anodes. The lithium metal anode with an IG current collector can achieve an average Coulombic efficiency of 97.5% in 100 cycles at current density of 1 mA cm<sup>-2</sup> and it can be cycled for over 300 h when assembled as symmetric cells with stable voltage profiles. This outstanding performance can be attributed to the large surface area of the IG network, sufficient ion channels provided by graphene hollow spheres, and excellent lithium dendrites suppression by the 2D graphene layers on the top. The morphological study also shows that after cycling the electrode surface is rather smooth and a stable SEI is formed, which is further confirmed by EIS measurement. These results indicate that the major challenge encountered in the development of lithium metal anodes, including safety risks and low Coulombic efficiency, can be resolved effectively. We believe this strategy can also be applied in other alkali metal anode like Na and full cells with various cathodes, implying huge practical application potential in energy storage field.

### 4. Experimental section

#### 4.1. Materials

Nickel spheres were purchased from US Research Nanomaterials Incorporation. The graphene oxide water dispersion was purchased from Graphenea Incorporation. The nickel etchant was purchased from Alfa Aesar. All chemicals were used as received.

#### 4.2. Preparation of 3D IG network

In a typical process, 100 mg of 1  $\mu$ m nickel microspheres was dispersed in 10 ml ethanol and was sonicated to form a uniform solution. 1 ml of graphene oxide water dispersion was then added into the solution and the mixed solution was stirred for 10 min. Vacuum filtration with the help of a vacuum pump was conducted immediately after stirring to form a flexible composite film. The film was punched into small circular disks with an area of 1.5 cm<sup>2</sup>, and then loaded into a one-inch quartz tube furnace. The furnace was first evacuated and filled with a mixture gas of 80 sccm Ar and 20 sccm H<sub>2</sub>. Then it was heated up to 850 °C in 15 min and was kept at this temperature for 10 min to anneal the films under 40 sccm Ar and 10 sccm H<sub>2</sub>. The small circular films were then exposed to 40 sccm Ar, 5 sccm CH<sub>4</sub> and 5 sccm H<sub>2</sub> for 10 min before they were cooled down to room temperature with a rate of 10 °C min<sup>-1</sup>. Few-layer graphene was grown on the surface of the nickel microspheres during this process. The as-prepared films were immersed in nickel etchant for certain minutes, washed with deionized water twice, and dried in ambient environment to form the 3D IG frameworks. The total mass of an IG circular disk is about 0.7 mg.

#### 4.3. Characterization

The morphology and the microstructure of the electrodes was characterized with a SEM (JEOL JSM-7001) operating at 10 kV and a TEM (JEOL 2100F). The element distribution was measured on the EDX attached to the TEM. Samples after cycling were washed with DOL/DME to remove the electrolyte residue and dried in an Ar-filled glovebox. The Raman spectroscopy measurement was carried out on a Renishaw inVia Raman microscope and the XPS data was measured

using a Kratos Axis Ultra XPS microprobe system to analyze the surface chemistry.

#### 4.4. Electrochemical measurements

For electrochemical testing, CR2032 coin cells were assembled in an Ar-filled glovebox with O<sub>2</sub> and H<sub>2</sub>O concentration below 0.1 ppm. The Network battery testing system and Gamry workstation were used to perform the measurements. The as-prepared 3D IG framework, a bare Cu foil, a Li metal foil were used as the modified electrode, the controlled electrode, and the counter electrode, respectively. Celgard 2400 was used as the separator and the electrolyte was the lithium bis(trifluoromethanesulfonyl)imide (LiTFSI) in 1,2-dimethoxyethane (DME) and 1,3-dioxolane (DOL) (volume ratio 1:1) with 0.2 M lithium nitrate (LiNO<sub>3</sub>) additive. The cycling test was carried out by discharging at 1.0 mA/cm<sup>2</sup> for 1 h and then charged to 1.0 V under the constant current density. For higher current rates, the cells were discharged at 2.0 mA cm<sup>-2</sup>, and then charged to 1.0 V at the same current.

### Acknowledgements

A portion of the images and data used in this article were generated at the Center for Electron Microscopy and Microanalysis, University of Southern California.

The EIS data used in this article was collected in Dr. Stephen Cronin's lab.

### Appendix A. Supporting information

Supplementary data associated with this article can be found in the online version at doi:10.1016/j.ensm.2018.09.028.

### References

- [1] K. Mizushima, P.C. Jones, P.J. Wiseman, J.B. Goodenough, Li<sub>x</sub>CoO<sub>2</sub> (0 < x < 1): a new cathode material for batteries of high energy density, *Mat. Res. Bull.* 15 (1980) 783–789.
- [2] A.K. Padhi, K.S. Nanjundaswamy, J.B. Goodenough, Phospho-olivines as positive-electrode materials for rechargeable lithium batteries, *J. Electrochem. Soc.* 144 (1997) 1188–1194.
- [3] B.M.L. Rao, R.W. Francis, H.A. Christopher, Lithium-aluminum electrode, *J. Electrochem. Soc. : Electrochem. Sci. Technol.* 124 (1977) 1490–1492.
- [4] X. Ji, K.T. Lee, L.F. Nazar, A highly ordered nanostructured carbon-sulphur cathode for lithium-sulphur batteries, *Nat. Mater.* 8 (2009) 500–506.
- [5] A. Manthiram, Y. Fu, Y.S. Su, Challenges and prospects of lithium-sulfur batteries, *Acc. Chem. Res.* 46 (2013) 1125–1134.
- [6] G. Zhou, S. Pei, L. Li, D.W. Wang, S. Wang, K. Huang, L.C. Yin, F. Li, H.M. Cheng, A graphene-pure-sulfur sandwich structure for ultrafast, long-life lithium-sulfur batteries, *Adv. Mater.* 26 (2014) 625–631 (664).
- [7] A. Zhang, X. Fang, C. Shen, Y. Liu, I.G. Seo, Y. Ma, L. Chen, P. Cottingham, C. Zhou, Functional interlayer of PVDF-HFP and carbon nanofiber for long-life lithium-sulfur batteries, *Nano Res.* (2017).
- [8] J. Wang, Y. Li, X. Sun, Challenges and opportunities of nanostructured materials for aprotic rechargeable lithium-air batteries, *Nano Energy* 2 (2013) 443–467.
- [9] G. Girishkumar, B. McCloskey, A.C. Luntz, S. Swanson, W. Wilcke, Lithium-air battery: promise and challenges, *J. Phys. Chem. Lett.* 1 (2010) 2193–2203.
- [10] K.F. Blurton, A.F. Sammells, Metal/air batteries: their status and potential – a review, *J. Power Sources* 4 (1979) 263–279.
- [11] S. Liang, Y. Hu, Z. Nie, H. Huang, T. Chen, A. Pan, G. Cao, Template-free synthesis of ultra-large V<sub>2</sub>O<sub>5</sub> nanosheets with exceptional small thickness for high-performance lithium-ion batteries, *Nano Energy* 13 (2015) 58–66.
- [12] X. Fang, F. Lin, D. Nordlund, M. Mecklenburg, M. Ge, J. Rong, A. Zhang, C. Shen, Y. Liu, Y. Cao, M.M. Doeff, C. Zhou, Atomic insights into the enhanced surface stability in high voltage cathode materials by ultrathin coating, *Adv. Funct. Mater.* 27 (2017) 1602873.
- [13] M. Ge, J. Rong, X. Fang, A. Zhang, Y. Lu, C. Zhou, Scalable preparation of porous silicon nanoparticles and their application for lithium-ion battery anodes, *Nano Res.* 6 (2013) 174–181.
- [14] C. Shen, M. Ge, A. Zhang, X. Fang, Y. Liu, J. Rong, C. Zhou, Silicon(lithiated)-sulfur full cells with porous silicon anode shielded by Nafion against polysulfides to achieve high capacity and energy density, *Nano Energy* 19 (2016) 68–77.
- [15] Y. Guo, H. Li, T. Zhai, Reviving lithium-metal anodes for next-generation high-energy batteries, *Adv. Mater.* 29 (2017).
- [16] S. Li, M. Jiang, Y. Xie, H. Xu, J. Jia, J. Li, Developing high-performance lithium

- metal anode in liquid electrolytes: challenges and progress, *Adv. Mater.* 30 (2018) e1706375.
- [17] Y.S. Cohen, Y. Cohen, D. Aurbach, Micromorphological studies of lithium electrodes in alkyl carbonate solutions using in situ atomic force microscopy, *J. Phys. Chem. B* 104 (2000) 12282–12291.
- [18] D. Lin, Y. Liu, Y. Cui, Reviving the lithium metal anode for high-energy batteries, *Nat. Nanotechnol.* 12 (2017) 194–206.
- [19] D. Aurbach, E. Zinigrad, H. Teller, P. Dan, Factors which limit the cycle life of rechargeable lithium (metal) batteries, *J. Electrochem. Soc.* 147 (2000) 1274–1279.
- [20] D. Aurbach, E. Zinigrad, Y. Cohen, H. Teller, A short review of failure mechanisms of lithium metal and lithiated graphite anodes in liquid electrolyte solutions, *Solid State Ion.* 148 (2002) 405–416.
- [21] M. Nie, B.L. Lucht, Role of lithium salt on solid electrolyte interface (SEI) formation and structure in lithium ion batteries, *J. Electrochem. Soc.* 161 (2014) A1001–A1006.
- [22] X.B. Cheng, R. Zhang, C.Z. Zhao, F. Wei, J.G. Zhang, Q. Zhang, A review of solid electrolyte interphases on lithium metal anode, *Adv. Sci. (Weinh.)* 3 (2016) 1500213.
- [23] C.P. Yang, Y.X. Yin, S.F. Zhang, N.W. Li, Y.G. Guo, Accommodating lithium into 3D current collectors with a submicron skeleton towards long-life lithium metal anodes, *Nat. Commun.* 6 (2015) 8058.
- [24] S.-S. Chi, Y. Liu, W.-L. Song, L.-Z. Fan, Q. Zhang, Prestoring lithium into stable 3D nickel foam host as dendrite-free lithium metal anode, *Adv. Funct. Mater.* 27 (2017) 1700348.
- [25] K. Yan, B. Sun, P. Munroe, G. Wang, Three-dimensional pie-like current collectors for dendrite-free lithium metal anodes, *Energy Storage Mater.* 11 (2018) 127–133.
- [26] X.-Y. Yue, W.-W. Wang, Q.-C. Wang, J.-K. Meng, Z.-Q. Zhang, X.-J. Wu, X.-Q. Yang, Y.-N. Zhou, CoO nanofiber decorated nickel foams as lithium dendrite suppressing host skeletons for high energy lithium metal batteries, *Energy Storage Mater.* 14 (2018) 335–344.
- [27] R. Zhang, X.R. Chen, X. Chen, X.B. Cheng, X.Q. Zhang, C. Yan, Q. Zhang, Lithiophilic sites in doped graphene guide uniform lithium nucleation for dendrite-free lithium metal anodes, *Angew. Chem. Int. Ed. Engl.* 56 (2017) 7764–7768.
- [28] X.B. Cheng, H.J. Peng, J.Q. Huang, R. Zhang, C.Z. Zhao, Q. Zhang, Dual-phase lithium metal anode containing a polysulfide-induced solid electrolyte interphase and nanostructured graphene framework for lithium-sulfur batteries, *ACS Nano* 9 (2015) 6373–6382.
- [29] D. Lin, Y. Liu, Z. Liang, H.W. Lee, J. Sun, H. Wang, K. Yan, J. Xie, Y. Cui, Layered reduced graphene oxide with nanoscale interlayer gaps as a stable host for lithium metal anodes, *Nat. Nanotechnol.* 11 (2016) 626–632.
- [30] A. Zhang, X. Fang, C. Shen, Y. Liu, C. Zhou, A carbon nanofiber network for stable lithium metal anodes with high Coulombic efficiency and long cycle life, *Nano Res.* 9 (2016) 3428–3436.
- [31] X. Ji, D.-Y. Liu, D.G. Prendiville, Y. Zhang, X. Liu, G.D. Stucky, Spatially heterogeneous carbon-fiber papers as surface dendrite-free current collectors for lithium deposition, *Nano Today* 7 (2012) 10–20.
- [32] T.T. Zuo, X.W. Wu, C.P. Yang, Y.X. Yin, H. Ye, N.W. Li, Y.G. Guo, Graphitized carbon fibers as multifunctional 3D current collectors for high areal capacity Li anodes, *Adv. Mater.* 29 (2017).
- [33] Z. Liang, D. Lin, J. Zhao, Z. Lu, Y. Liu, C. Liu, Y. Lu, H. Wang, K. Yan, X. Tao, Y. Cui, Composite lithium metal anode by melt infusion of lithium into a 3D conducting scaffold with lithiophilic coating, *PNAS* 113 (2016) 2862–2867.
- [34] Y. Zhang, B. Liu, E. Hitz, W. Luo, Y. Yao, Y. Li, J. Dai, C. Chen, Y. Wang, C. Yang, H. Li, L. Hu, A carbon-based 3D current collector with surface protection for Li metal anode, *Nano Res.* 10 (2017) 1356–1365.
- [35] F. Shen, F. Zhang, Y. Zheng, Z. Fan, Z. Li, Z. Sun, Y. Xuan, B. Zhao, Z. Lin, X. Gui, X. Han, Y. Cheng, C. Niu, Direct growth of 3D host on Cu foil for stable lithium metal anode, *Energy Storage Mater.* 13 (2018) 323–328.
- [36] L. Liu, Y.-X. Yin, J.-Y. Li, N.-W. Li, X.-X. Zeng, H. Ye, Y.-G. Guo, L.-J. Wan, Free-standing hollow carbon fibers as high-capacity containers for stable lithium metal anodes, *Joule* 1 (2017) 563–575.
- [37] G. Zheng, S.W. Lee, Z. Liang, H.W. Lee, K. Yan, H. Yao, H. Wang, W. Li, S. Chu, Y. Cui, Interconnected hollow carbon nanospheres for stable lithium metal anodes, *Nat. Nanotechnol.* 9 (2014) 618–623.
- [38] K. Yan, H.W. Lee, T. Gao, G. Zheng, H. Yao, H. Wang, Z. Lu, Y. Zhou, Z. Liang, Z. Liu, S. Chu, Y. Cui, Ultrathin two-dimensional atomic crystals as stable interfacial layer for improvement of lithium metal anode, *Nano Lett.* 14 (2014) 6016–6022.
- [39] E. Cha, M.D. Patel, J. Park, J. Hwang, V. Prasad, K. Cho, W. Choi, 2D MoS<sub>2</sub> as an efficient protective layer for lithium metal anodes in high-performance Li-S batteries, *Nat. Nanotechnol.* 13 (2018) 337–344.
- [40] X. Li, W. Cai, L. Colombo, R.S. Ruoff, Evolution of graphene growth on Ni and Cu by carbon isotope labeling, *Nano Lett.* 9 (2009) 4268–4272.
- [41] Z. Chen, W. Ren, L. Gao, B. Liu, S. Pei, H.M. Cheng, Three-dimensional flexible and conductive interconnected graphene networks grown by chemical vapour deposition, *Nat. Mater.* 10 (2011) 424–428.
- [42] W. Jiang, H. Xin, W. Li, Microcellular 3D graphene foam via chemical vapor deposition of electroless plated nickel foam templates, *Mater. Lett.* 162 (2016) 105–109.
- [43] Z. Chen, C. Xu, C. Ma, W. Ren, H.M. Cheng, Lightweight and flexible graphene foam composites for high-performance electromagnetic interference shielding, *Adv. Mater.* 25 (2013) 1296–1300.
- [44] I.K. Moon, J. Lee, R.S. Ruoff, H. Lee, Reduced graphene oxide by chemical graphitization, *Nat. Commun.* 1 (2010) 73.
- [45] A.C. Ferrari, J.C. Meyer, V. Scardaci, C. Casiraghi, M. Lazzeri, F. Mauri, S. Piscanec, D. Jiang, K.S. Novoselov, S. Roth, A.K. Geim, Raman spectrum of graphene and graphene layers, *Phys. Rev. Lett.* 97 (2006) 187401.
- [46] D. Yang, A. Velamakanni, G. Bozoklu, S. Park, M. Stoller, R.D. Piner, S. Stankovich, I. Jung, D.A. Field, C.A. Ventrice, R.S. Ruoff, Chemical analysis of graphene oxide films after heat and chemical treatments by X-ray photoelectron and Micro-Raman spectroscopy, *Carbon* 47 (2009) 145–152.
- [47] K. Yan, Z. Lu, H.-W. Lee, F. Xiong, P.-C. Hsu, Y. Li, J. Zhao, S. Chu, Y. Cui, Selective deposition and stable encapsulation of lithium through heterogeneous seeded growth, *Nat. Energy* 1 (2016) 16010.
- [48] C. Yang, Y. Yao, S. He, H. Xie, E. Hitz, L. Hu, Ultrafine silver nanoparticles for seeded lithium deposition toward stable lithium metal anode, *Adv. Mater.* 29 (2017).
- [49] N. Nitta, F. Wu, J.T. Lee, G. Yushin, Li-ion battery materials: present and future, *Mater. Today* 18 (2015) 252–264.
- [50] N.W. Li, Y.X. Yin, C.P. Yang, Y.G. Guo, An artificial solid electrolyte interphase layer for stable lithium metal anodes, *Adv. Mater.* 28 (2016) 1853–1858.
- [51] N.W. Li, Y. Shi, Y.X. Yin, X.X. Zeng, J.Y. Li, C.J. Li, L.J. Wan, R. Wen, Y.G. Guo, A flexible solid electrolyte interphase layer for long-life lithium metal anodes, *Angew. Chem. Int. Ed. Engl.* 57 (2018) 1505–1509.
- [52] R. Miao, J. Yang, X. Feng, H. Jia, J. Wang, Y. Nuli, Novel dual-salts electrolyte solution for dendrite-free lithium-metal based rechargeable batteries with high cycle reversibility, *J. Power Sources* 271 (2014) 291–297.
- [53] X.Q. Zhang, X. Chen, X.B. Cheng, B.Q. Li, X. Shen, C. Yan, J.Q. Huang, Q. Zhang, Highly stable lithium metal batteries enabled by regulating the solvation of lithium ions in nonaqueous electrolytes, *Angew. Chem. Int. Ed. Engl.* 57 (2018) 5301–5305.